Temporal and spatial dynamics of paleo-redox conditions across the Triassic-Jurassic boundary

Ashley N. Prow[1], Zunli Lu[1], Clara L. Blättler[2], Tianchen He[3], Zonglin Yang[1], Pulkit Singh[4], Preston Cosslett Kemeny[2], Jordan P. Todes[2], Alexandre Pohl[5], Tripti Bhattacharya[1], Bas van de Schootbrugge[6], Paul B. Wignall[7], Jonathan L. Payne[4]

(1) Department of Earth and Environmental Sciences, Syracuse University, New York, USA

(2) Department of the Geophysical Sciences, University of Chicago, Illinois, USA

(3) College of Oceanography, Hohai University, Nanjing, China

(4) Department of Earth and Planetary Sciences, Stanford University, California, USA

(5) Biogéosciences, UMR 6282 CNRS, Université de Bourgogne, Dijon, France

(6) Department of Earth Sciences, Utrecht University, Utrecht, The Netherlands

(7) School of Earth and Environment, University of Leeds, Leeds, UK

Key Points

- Calcium isotope ratios were measured for two carbonate successions in Italy spanning the Triassic-Jurassic boundary interval
- Paired proxy data indicate the sites underwent different modes of diagenetic alteration but retain some primary redox signals
- Ocean circulation strength and depth of vertical mixing may explain the difference in local redox conditions

Abstract

The end-Triassic mass extinction was among the most severe biotic crises of the Phanerozoic. It has been linked with the global expansion of marine anoxia, and the prolongation of these conditions within epeiric seas has been proposed as a cause for the suppression of biodiversity during the Hettangian. Testing this interpretation is complicated by spatially heterogenous patterns of local marine redox conditions within the western Tethys European Epicontinental Shelf. In this study we assess the redox state within this region by focusing on two carbonate successions in Italy. Based on I/Ca ratios, these locations record distinct local background redox conditions, with Val Adrara showing notably lower pre-extinction oxygen saturation state compared to Mount Sparagio. To better explain these differences, $\delta^{44}Ca$ and trace element analyses were used to identify the roles of mineralogical and diagenetic effects on the preservation of primary redox signals. A framework of multiple elemental (Sr, Mg, Mn, I) and isotopic ($\delta^{13}C$, $\delta^{18}O$, $\delta^{44}Ca$, $\delta^{238}U$ and $\delta^{34}S_{CAS}$) ratios was developed to identify factors that could influence carbonate geochemistry. Both sites probably retain some primary variation in $\delta^{238}U$, $\delta^{34}S_{CAS}$ and I/Ca, but they are likely also shaped by changing mineralogy and early diagenetic conditions which complicates interpretations of the seawater composition. Where the redox signals are largely preserved, we interpret differences in pre-extinction I/Ca between the two sites to reflect distinct local oxygenation states. Model simulations show that ocean circulation and hydrological regime could have been important drivers of spatial heterogeneity in paleo-redox conditions across the European Epicontinental Shelf.

Plain Language Summary

The end-Triassic mass extinction, 200 million years ago, may have been caused by rapid injection of large quantities of carbon from volcanoes analogous to modern-day fossil fuel consumption. The main killing mechanism may have been anoxia, or low dissolved oxygen content, in the shallow ocean. Understanding the distribution of dissolved oxygen in the shallow ocean where many organisms live is imperative for predicting future ecosystem sustainability. Carbonate sediments record the chemical composition of seawater upon deposition, preserving information about ancient ocean conditions Several carbonate-based geochemical proxies can be used to infer the oxygen saturation state in the ocean, but their values can be altered by post-depositional processes. During the Triassic, Europe was inundated with a shallow sea where carbonate limestone deposition occurred, but the local seawater composition differs between two sites in Italy. We use the carbonate calcium isotope ratios, which are sensitive to post-depositional alteration, to investigate the effect of alteration on the proxy signals. While alteration influences the absolute values of the seawater composition preserved at the two sites, the overall trends in oxygen saturation are distinct and mostly unaltered. Earth system modeling suggests that the difference between sites may be due to ocean circulation and hydrological patterns.

1. Introduction

The end-Triassic mass extinction (~200 Ma) was among the most important biotic crises of the Phanerozoic, resulting in the loss of nearly 20% of marine animal families (Bambach, 2006; Kiessling et al., 2007). Losses were severe amongst many groups, especially scleractinian corals, which lost up to 96% of their genera (Hautmann, 2006). The disappearance of characteristic Triassic fauna closely coincides with an abrupt negative carbon-isotope ($\delta^{13}C_{org}$) excursion in organic matter of up to -5 ‰ (Hesselbo et al., 2002; van de Schootbrugge et al., 2008; Bachan et al., 2016; Wignall and Atkinson 2020). The negative $\delta^{13}C_{org}$ excursion is contemporaneous with the emplacement of the Central Atlantic Magmatic Province (CAMP) (Schoene et al., 2010; Blackburn et al., 2013) suggesting a scenario of rapid injection (< 20 ka) of highly depleted carbon (up to -70 ‰) followed by the enhanced burial of organic carbon leading to a prolonged positive excursion (Hesselbo et al, 2002; Bachan et al., 2016). Recovery of marine communities was spatially variable, being notably rapid in nearshore communities in NW Europe (Atkinson and Wignall 2019) but skeletal abundance remains suppressed until the Sinemurian in Tethyan carbonates (Singh et al., 2023).

Enrichment of redox-sensitive elements and the restructuring of microbial communities support widespread marine anoxia as a kill mechanism (van de Schootbrugge et al., 2008; Wignall and Atkinson 2020; He et al., 2020a; Beith et al., 2021; Onoue et al., 2022). Understanding the extent and degree of deoxygenation in the shallow ocean (<100 m), where most organisms live, is essential to assessing the ecological impacts of the event. Carbonate-based water-column redox proxies show heterogeneous spatial patterns of deoxygenation within the European Epicontinental Shelf (EES) along the western margin of the Tethys Ocean (Fig. 1) (e.g., Luo et al., 2018; He et

al., 2022a; Singh et al., 2023), raising questions about whether some have been diagenetically altered or if they record original spatial variation.

In this study, we focus on two locations: Mount Sparagio in Sicily and Val Adrara in the Lombardy Basin of the southern Italian Alps (Fig. 1). The peritidal carbonate succession at Mount Sparagio, in the southeastern region of the EES, records an abrupt positive shift in carbonate-associate sulfur isotope ($\delta^{34}S_{CAS}$) ratios coincident with the extinction interval, indicating a rapid and intense onset of global anoxia commencing near the Triassic-Jurassic boundary (Fig. 2; He et al. 2020). This signature correlates with a negative excursion in carbonate-phase $\delta^{238}U$, another indicator of global anoxia, recorded in the shallow carbonate ramp deposits at the Val Adrara (Fig. 3; Jost et al., 2017).

Carbonate-hosted, redox-sensitive elemental and isotopic ratios can track seawater composition (Kampschulte and Strauss, 1996; Zhang et al., 2020). The variations in seawater $\delta^{34}S$ and $\delta^{238}U$ compositions are controlled by the burial fluxes under reducing conditions and the size of the seawater reservoir (Bottrell and Newton, 2006; Chen et al., 2021). Microbial sulfate reduction occurring under anoxic conditions imparts a large negative fractionation in the available sulfate by preferential incorporation of the lighter ^{32}S isotope into sulfide minerals, thus leaving the seawater sulfate pool enriched in ^{34}S (Kampschulte and Strauss, 2004; Sim. et al., 2011). The reduced form of uranium (U^{4+}) is less soluble than the oxidized form (U^{6+}). The preferential removal of ^{238}U in anoxic settings leads to its depletion in the seawater pool (Zhang et al., 2020). Consequently, the isotopic signatures of both $\delta^{238}U$ and $\delta^{34}S_{CAS}$ recorded in carbonate respectively decrease and increase in response to expanding seafloor anoxia. The magnitudes of their isotopic offsets from seawater values are often considered to reflect the global extent of anoxia (Fike et al., 2015; Zhang et al., 2020; Chen et al., 2021). Iodate (IO_3^-), the oxidized form of iodine, can be

incorporated into the calcite lattice whereas the reduced form iodide (I^-) is excluded (Lu et al., 2020). Iodate is rapidly reduced under low-oxygen conditions, so that low I/Ca likely reflects carbonate accumulation beneath dysoxic-anoxic water masses (Lu et al., 2020).

While both Val Adrara and Mount Sparagio record signals of enhanced global extent of anoxic settings during the positive $\delta^{13}C$ excursion, the local seawater conditions, as indicated by I/Ca (or I/(Ca+Mg)), are distinct (He et al., 2022a; Singh et al., 2023). Background I/Ca values prior to the positive excursion at Mount Sparagio are elevated relative to Val Adrara (Figs. 2 and 3). During the excursion, I/Ca values decrease to near zero at Val Adrara. At Mount Sparagio, the highly variable background I/Ca values only reduce to between 1-2 μmol/mol, higher still than the pre-excursion values at Val Adrara. We explore whether the discrepancy in local expressions of the I/Ca signal along the northern and southern EES margins reflects diagenetic overprinting, differences in original mineralogy, or contrasting primary redox conditions.

Calcium isotope ratios ($^{44}Ca/^{40}Ca$, commonly reported as $\delta^{44}Ca$) are a versatile tool for constraining post-depositional processes, such as dolomitization or recrystallization (Fantle et al., 2020), and for fingerprinting the effects of different primary carbonate minerals (Higgins et al., 2018). At low-temperature conditions, kinetic isotope effects are believed to dominate, with important rate-dependent fractionation of Ca isotopes into different calcium-bearing mineral phases (Tang et al., 2008). Under slow precipitation rates, such as may occur during authigenic or diagenetic carbonate precipitation, no appreciable fractionation may be observed (Fantle and DePaolo, 2007; Jacobson and Holmden, 2008). Thus, $\delta^{44}Ca$ can be used to track the diagenetic history of carbonates. In addition, calcite and aragonite exhibit different fractionations (Gussone et al., 2003), which makes $\delta^{44}Ca$ a potentially useful indicator of primary carbonate mineralogy. Here, $\delta^{44}Ca$ measurements are employed to examine the role of local mineralogical and diagenetic

effects on the preservation state of carbonate-based redox proxies ($\delta^{238}U$, $\delta^{34}S_{CAS}$, I/Ca). We first investigate the presence of co-variability of $\delta^{44}Ca$ with other elemental components (Sr/Ca, Mg/Ca, Mn/Sr) considered diagnostic of different diagenetic and source-mixing regimes. These analyses allow us to test the robustness of the redox gradient in the EES. Then, we discuss potential drivers of the spatial redox pattern in the EES based on simulations conducted with the Community Earth System model.

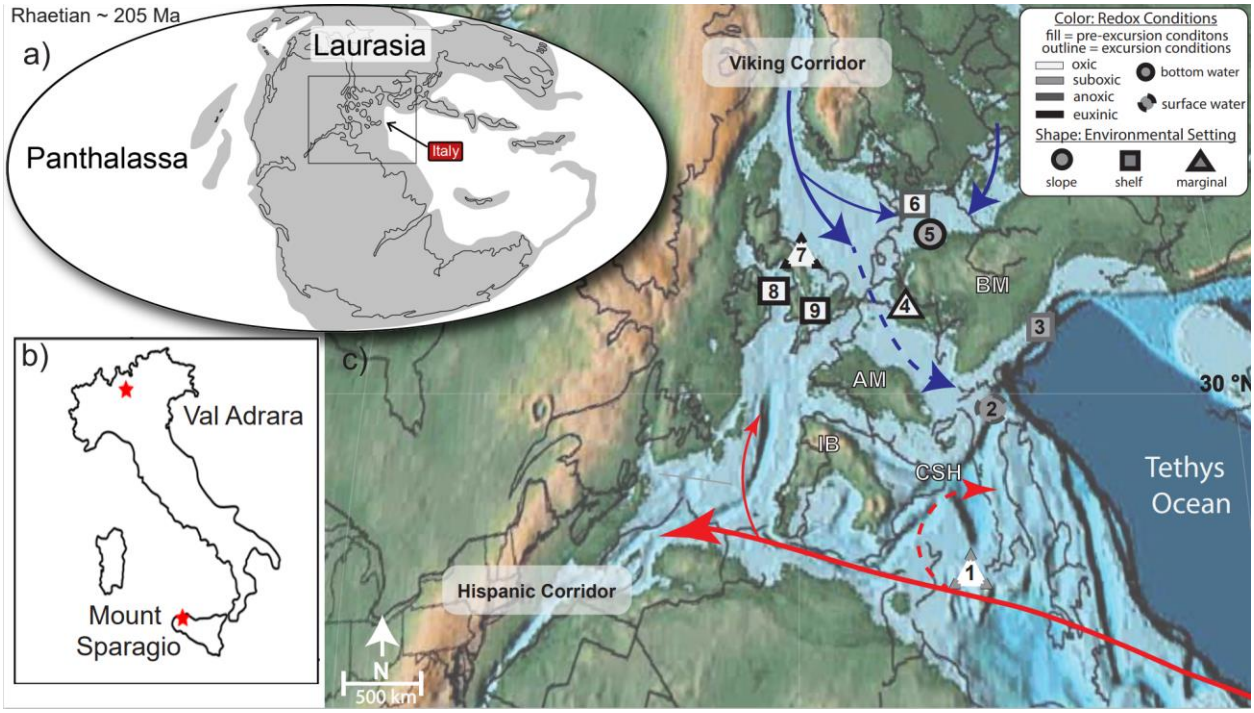

Figure 1: Paleo-geographical context of EES during the Late Triassic Rhaetian stage (~205 Ma). (A) Paleogeographic reconstruction of Pangaea, highlighting the location of the EES (box) and approximate location of modern-day Italy. (B) Site locations on map of modern Italy modified from Bachan et al. (2012). (C) Map of the northwestern Tethys epeiric sea. Arrows indicate proposed circulation pathways accounting for speculative bathymetry and emerged landmasses, and arrow color distinguishes between cool water (blue) and warm water (red). The thickness of the arrow indicates the current strength. Dotted lines are proposed flow paths modified from Ruvalcaba Baroni et al. (2018) with considerations based on CESM 1.2.2 simulations for the Triassic-Jurassic and Rhaetian configurations (Scotese, 2014). Modern-day geographic coordinates were rotated to paleo-coordinates using the R package Chronosphere and the Scotese PALEOMAP reconstruction (Kocsis and Raja, 2023; Scotese and Wright, 2018). IB: Iberian

Mountains, AM: Amorican, BM: Bohemian Massif, CSH: Corsican-Sardinian High. 1: Mount Sparagio, Italy (Todaro et al., 2018), 2. Val Adrara, Italy (van de Schootbrugge et al., 2008), 3. Kuhjoch, Austria (Li et al., 2022b), 4. Rosswinkel, Luxembourg (Richoz et al., 2012), 5. Mingolshiem, Germany (Luo et al., 2018), 6. Mariental, Germany (Richoz et al., 2012). 7. Filikirk, United Kingdom (Beith et al., 2021), 8. St. Audrie's, United Kingdom (Li et al., 2022b), 9. Doniford Bay, UK (Paris et al., 2010). See Table S3, supplementary materials for literature summary of redox conditions at these sites.

2. Methods

2.1. Study Site and Geological Setting

Approximately centered at 30°N paleolatitude, the EES was a warm, semi-restricted collection of silled basins and carbonate platforms during the early Mesozoic. Fragmentation of Pangaea permitted limited water exchange between the Boreal, Tethys, and the Panthalassa Ocean to the west (Fig. 1), although the precise timing of connection and amount of exchange in the Late Triassic are poorly constrained (Dore, 1991; Sha, 2002, Korte et al. 2015). Italy was mostly submerged in the southeastern region of the EES during the Triassic-Jurassic boundary interval, but intermittent subaerial exposure is evident in both Sicilian and Tuscan sections (Fig. 1) (Santantonio and Carminati, 2011; Bernardi et al., 2018).

2.1.2. Stratigraphy of Mount Sparagio

The Rhaetian to lower Hettangian succession at Mount Sparagio was deposited in a peritidal setting with intermittent subaerial exposure (Fig. 2) (Todaro et al., 2018). The studied section at Mount Sparagio is subdivided into three units: A, B, and C (Todaro et al., 2018). Units A (below the studied section) and B are assigned to Rhaetian age based on the occurrence of megalodontids and the benthic foraminiferan *Triasina hantkeni*. These lower units are characterized by the stacking of shallowing-upward cycles capped by red paleosols. Unit C lacks

the large megalodontid bivalves (Todaro et al., 2018). There is an approximately 20 m-thick barren interval capping unit B, concurrent with the onset of anoxia in the basin (He et al., 2022; He et al., 2020). Unit C is dated to the early Hettangian due to the absence of *T. hantkeni* and the occurrence of *Thaumatoporella parvovesiculifera* (Todaro et al., 2018). Unit C sediments were deposited in slightly deeper waters than the lower units and lacks paleosols.

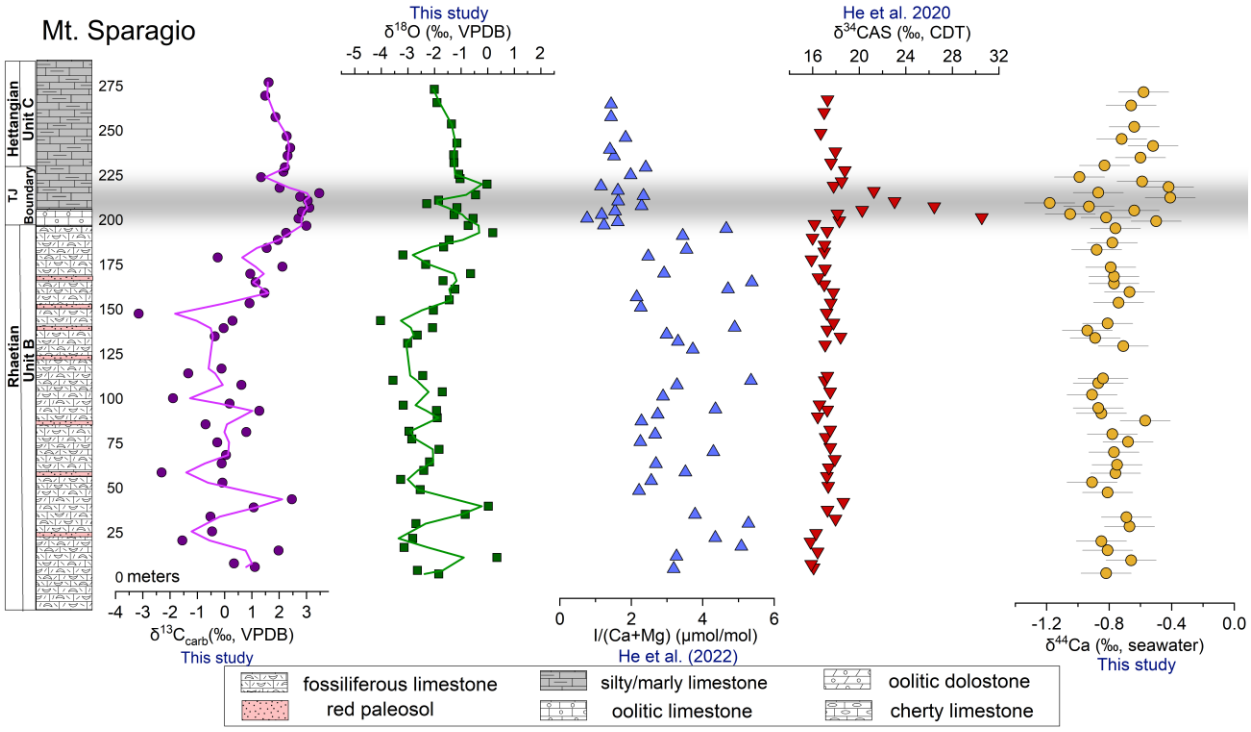

Figure 2: Chemo-stratigraphy and redox trends at Mount Sparagio (modern coordinates: 38°3′ 44.18″ N, 12°43′9.19″ E). The grey bar indicates the extinction interval. Solid lines trending with carbon and oxygen isotope ratios are loess smoothing regressions.

2.1.3. Stratigraphy of Val Adrara

The Val Adrara site is in the Lombardy Basin of the Southern Italian Alps (Jadoul and Galli, 2008; Bachan et al., 2012). Sedimentary sequences at Val Adrara record deposition on a passive-margin carbonate ramp (Santantonio and Carminati, 2011) and are assigned Rhaetian

through Hettangian ages based on palynological associations and carbon-isotope stratigraphy (Fig. 3; van de Schootbrugge et al., 2008). The lowermost Rhaetian-age Zu Formation is a fossiliferous packstone consisting of an unrestricted marine assemblage. It is abruptly overlain by the Malanotte Formation, which is devoid of fossils and is interpreted as the extinction interval (Fig. 3; Jadoul and Galli, 2008; Bachan et al., 2012). The lower Malanotte consists of thinly bedded micritic limestone (marl), which grades into carbonate-rich mud and wackestones (Jadoul and Galli, 2008). The negative excursion in $\delta^{13}C_{carb}$, with a magnitude of -5.0 ‰, coincides with the extinction interval and occurs entirely within lower silty-marl portion of the Malanotte Formation (van de Schootbrugge et al., 2008; Bachan et al., 2012). The silty marl layer of the lower Malanotte Formation is most likely correlative with the marly layer at Sparagio (Todaro et al. 2022). However, neither site has been absolutely dated, so the timing and duration of this interval is poorly constrained (Bachan et al. 2012; Todaro et al. 2018). Therefore, in both stratigraphic columns this interval is not assigned to either the Rhaetian or Hettangian and is broadly referred to as the Triassic-Jurassic boundary interval (Fig. 2 and 3). The negative excursion is followed by a small positive excursion terminating at the top of the Malanotte Formation. The overlying Albenza Formation is composed of 100 m of cross-bedded oolitic and peloidal grainstones interbedded with cm-scale layers of dolomicrite (Bachan et al., 2012). Another pulse of volcanism is inferred from a second -4.0 ‰ negative carbon isotope excursion at the base of the Albenza Formation and the protracted positive carbon-isotope excursion that follows terminates at the top of the Albenza Formation (Bachan et al., 2012; Bachan and Payne, 2016). Evidence of expanded global anoxia commences during this positive excursion and may have suppressed faunal recovery in this region (Singh et al. 2023). The Albenza Formation is sparsely fossiliferous with skeletal grains only become abundant again at the Albenza-Sedrina contact (Singh et al. 2023). The lower Sedrina

consists of packstone and grades into a thinly bedded cherty limestone with abundant sponge spicules (van de Schootbrugge et al., 2008; Singh et al., 2023). The upper Sedrina is interpreted to have been deposited below storm wave base following rapid subsidence due to the onset of extensional activity in the Hettangian (Santantonio and Carminati, 2011).

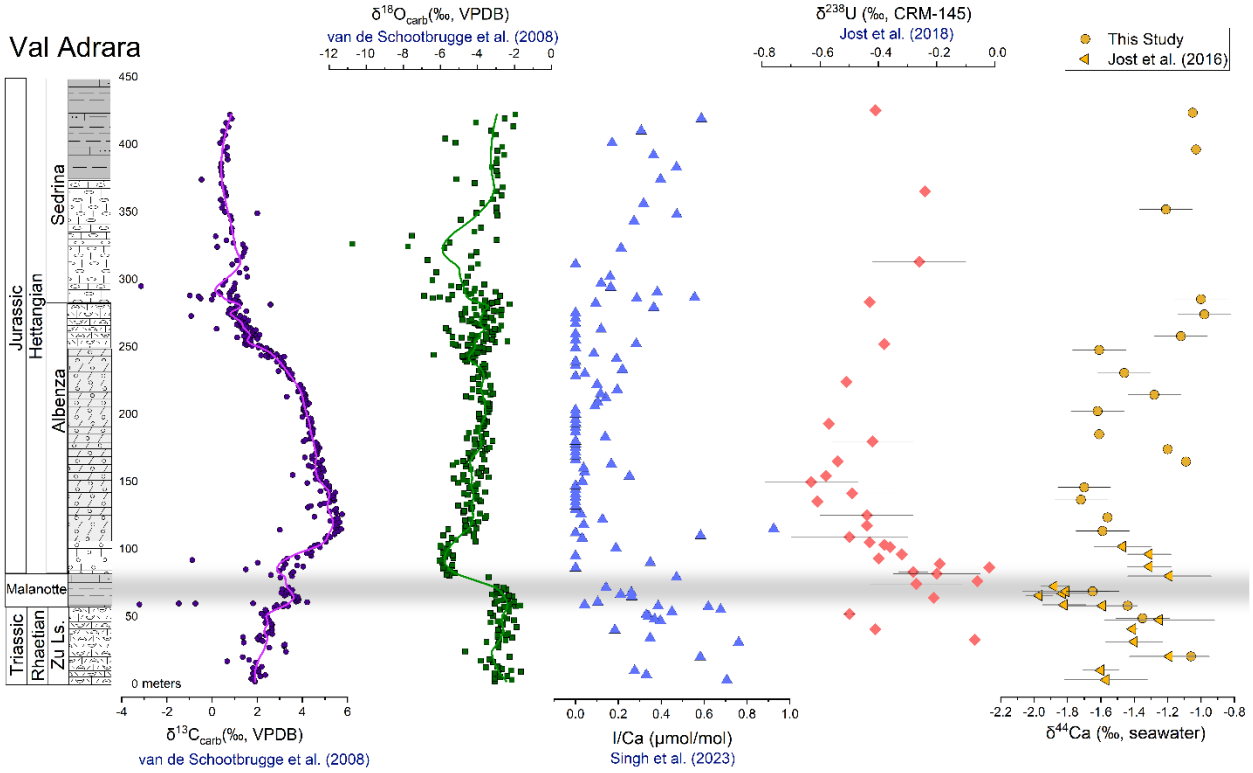

Figure 3: Chemostratigraphic trends at Val Adrara (modern coordinates: 45°43′29.33″N 9°57′32.29″E). Error bars for $\delta^{238}U$ and $\delta^{44}Ca$ are 2σ. See Fig. 2 for lithologic key.

2.2. Sample Preparation and Analysis

Published geochemical data were compiled to compare redox trends at the sites (Figs. 2 and 3). These data include carbon- and oxygen-isotope profiles for the Val Adrara section (van de Schootbrugge et al., 2008), estimates of global anoxia from $\delta^{34}S_{CAS}$ at Mount Sparagio (He et al., 2020), and from $\delta^{238}U$ at Val Adrara (Jost et al., 2017), and I/Ca at Val Adrara and I/(Ca+Mg) from Mount Sparagio as indicators of local redox conditions (He et al., 2022a; Singh et al., 2023).

Calcium-isotope data on different powered samples from the upper Zu limestone and Malanotte Formation were previously reported in Jost et al. (2016). These data bracket the negative carbon isotope excursion, but only include the rising limb of the subsequent positive excursion (Fig. 3). Here we report bulk carbonate $\delta^{44}Ca$ and trace elemental (Sr, Mn, Mg) concentrations data that span the full stratigraphic range for both sites (Fig. S2 and S3, supplementary materials). We also measure carbon- and oxygen-isotope compositions for new samples from Mount Sparagio (n = 52).

2.2.1. Carbon and oxygen isotope measurements

For samples from the Mount Sparagio section, about 10 mg of carbonate powder were drilled from the cleaned rock slab using a hand drill. Powder was reacted with 100% H_3PO_4 at 70 °C to extract CO_2 for $^{13}C/^{12}C$ and $^{18}O/^{16}O$ measurements. We used the Chinese national standard, an Ordovician carbonate from a site near Beijing (reference number GBW04405, $\delta^{13}C$ = 0.57 ± 0.03 ‰ VPDB; $\delta^{18}O$ = -8.49 ± 0.13 ‰ VPDB) to monitor the accuracy. These measurements were performed using a Finnigan MAT 253 mass spectrometer in the Nanjing Institute of Geology and Palaeontology.

2.2.2. Calcium isotope ratios and trace elemental analysis

Measurement of carbonate $\delta^{44}Ca$ values at the University of Chicago closely followed the method of Razionale et al. (2022). Briefly, carbonate samples were dissolved in buffered acetic acid at a ratio of ~1 mg/mL and Ca^{2+} was chromatographically isolated using a Dionex ICS-6000 with variable strength MSA eluent. Samples were matrix matched at 1 ppm Ca^{2+} in 2% nitric acid for sample-standard bracketing and each post-chromatography eluent was measured twice by Neptune XT as 90 integration cycles monitoring masses 42, 43, 43.5, and 44. Outlier cycles

exceeding ±3σ for the $^{44}Ca/^{42}Ca$, $^{44}Ca/^{43}Ca$, or $^{43}Ca/^{42}Ca$ intensity ratios were removed, as were entire sets of cycles when the $^{44}Ca/^{42}Ca$ ratio of successive bracketing standards changed by >0.2‰. Following a correction for strontium interference and a run-specific concentration effect, values of $\delta^{44/42}Ca$ were corrected to NIST 915b and scaled to $\delta^{44/40}Ca$ ratios using a kinetic mass law (Young et al., 2002) and assuming no radiogenic ^{40}Ca-excess. Samples are reported relative to seawater by setting the $\delta^{44/40}Ca$ value of 915b equal to -1.15‰. Measurements were only considered successful if the two final $\delta^{44/40}Ca$ determinations on the same post-column solution were within 0.2‰. Accuracy and precision were confirmed through measurement of $\delta^{44/40}Ca$ values in Princeton University Aragonite (PUA), measured as -1.42 ± 0.17‰ (2σ, n = 30), and of San Salvador Sand (SSS), measured as -1.31 ± 0.15‰ (2σ, n = 28). The precision of 915b measurements (±0.16‰, 2σ, n = 40) agreed with these reference materials; furthermore, for samples chromatographically isolated at least twice (36/49), two times the mean standard deviation in replicate $\delta^{44/40}Ca$ values was 0.15‰. Precision for each sample is reported as the largest of either replicate measurements or the mean reproducibility of 915b, PUA, and SSS (±0.16‰, 2σ).

2.2.3. Trace metal concentrations

A suite of major- and trace-element abundances were measured using a Thermo Scientific iCAP RQ inductively-coupled plasma mass spectrometer (ICP-MS) at the University of Chicago, following a standard geochemical protocol as described in Bryant et al. (2022). In brief, small aliquots of the dissolved samples were subsampled, adjusted to approximately 10 ppm Ca in 2% HNO_3 prior to analysis to mitigate matrix effects, and spiked with an internal standard solution containing Sc, Y, and In. At the beginning of each run, a calibration curve was generated for each element to calculate elemental concentrations. Calibration standards, calibration blanks, and duplicate samples were analyzed intermittently throughout each run for quality control. V, Cr, Mn,

and Fe ratios are reported from analytical runs in Kinetic Energy Discrimination (KED) mode, while Sr, U, and Mg ratios are reported from analytical runs in Standard (STD) mode. Data are reported as molar ratios to Ca + Mg. In addition, Mg/(Mg+Ca) ratios were independently measured via ion chromatography during chromatographic separation of calcium, as outlined above.

3. Results

At Val Adrara prior to the onset of the positive carbon-isotope excursion, $\delta^{44}Ca$ composition steadily decreases from -1.0‰ in the upper Zu limestone to a minimum of −1.65 ‰ in the Malanotte Formation in our new dataset (Fig. 3, Table S1). Calcium isotope ratios were measured for two samples at the same stratigraphic heights at Val Adrara as Jost et al. (2016) with one at 20 m in the Zu limestone and the other at 67.2 m in the Malanotte Formations. Both have a systematic offset of about 0.14 ‰ with these new data being more positive. A shift toward lower $\delta^{44}Ca$ is observed in the Malanotte in both datasets (Fig. 3). During the positive $\delta^{13}C$ excursion in the Albenza Formation, $\delta^{44}Ca$ values are highly variable between –1.72 ‰ and –1.20 ‰. A gradual trend toward more positive $\delta^{44}Ca$ values, ranging from –1.12 ‰ to –0.98 ‰, occurs at the lithological change from oolitic grainstone to fossiliferous packstone in the upper Albenza Formation.

At Mount Sparagio, pre-excursion $\delta^{44}Ca$ values have relatively small variability, ranging from –0.57 ‰ to –0.91 ‰ (Table S1) and are enriched relative to Val Adrara. The $\delta^{44}Ca$ values begin to fluctuate rapidly with a spread from –1.10 ‰ to –0.40 ‰ at the same time as the increase in $\delta^{34}S_{CAS}$ and decrease in I/(Ca+Mg). The carbon isotopic composition of unit B at Mount Sparagio is highly variable, with $\delta^{13}C$ values ranging from –3.15 ‰ to 2.46 ‰ (Table S1). A positive trend emerges approximately 50 m below the inferred extinction window at the top of unit B and

continues through the end of the record, peaking at a value of 3.04 ‰ (Table S2). A corresponding positive trend is also observed in the $\delta^{18}O$ record.

Minor- and trace-element concentrations at Mount Sparagio are relatively uniform throughout with the exception of the Triassic-Jurassic boundary interval where Mg, Sr, Mn, U, and V concentrations, all normalized to (Ca+Mg), increase by almost an order of magnitude then decrease to pre-excursion values (Fig. S1). There is a step decrease in Cr/(Ca+Mg) from an average of ~5.5 μmol/mol to 2.5 μmol/mol at the boundary. At Val Adrara, Mg/(Ca+Mg) ratios remain lower than 0.1 mol/mol throughout with only one value at ~175 m in the Albenza Formation that is elevated in both Mg/(Ca+Mg) (~0.4 mol/mol) and Mn/(Ca+Mg) (~0.3 mmol/mol). Redox sensitive trace elements Mn, V, and Cr decrease at the boundary interval in the Malanotte Formation. V and Cr/(Ca+Mg) remain low for the lower 100 m of the Albenza Formation and then begin trending toward pre-excursion values. Mn/(Ca+Mg) remains low until the Sedrina Formation. Sr/(Ca+Mg) are overall higher than at Mount Sparagio (~1 mmol/mol) with some elevated values (~3 mmol/mol) during the Malanotte Formation.

4. Discussion

Here we integrate published geochemical datasets with newly measured $\delta^{44}Ca$ values to constrain the impact of sedimentary processes, mineralogy, and diagenesis on these three redox proxy signals. By building a framework of geochemical tracers with differential responses and sensitivities to diagenetic regimes (Table 1), potential influences of lithification processes on primary redox signals can be teased apart. In terms of I/Ca, we aim to investigate (1) whether the deoxygenation trend observed at both sites is the result of diagenetic loss of carbonate-associated iodate; and (2) whether the overall low I/Ca at Val Adrara could be the result of more severe diagenesis compared to Mount Sparagio.

4.1. Review of diagenetic redox proxies

Table 1 summarizes the predicted directional changes in isotopic and elemental compositions of a primary carbonate initially formed under normal-marine conditions undergoing one of two modes of diagenesis (sediment- and fluid-buffered) and one of four fluid compositions (meteoric, seawater, evaporitic brine, and reducing pore fluid). The table is structured in this manner to highlight contrasting susceptibilities to alteration under different diagenetic environments of non-stoichiometric redox-sensitive elements compared to that of major constituents. Covariation between two (or three) paleo-proxies can elucidate the complex post-depositional history of the sediment and fidelity of the original signal (Fantle et al., 2020).

Table 1: Summary of expected response of tracers under different conditions. Symbol key: Up arrow (↑) indicates isotopically heavier or more positive. Down arrow (↓) indicates isotopic lighter or more negative. The number of arrows indicates the sensitivity of the proxy to that process/mode of diagenesis. A dash (–) indicates that the proxy is largely unaffected by the process. Sources: $\delta^{13}C$ and $\delta^{18}O$ (Oehlert and Swart, 2014; Ahm et al., 2018; Swart and Oehlert, 2018; Reis et al., 2019), $\delta^{44}Ca$ (Fantle and Higgins, 2014; Kimmig and Holmden, 2017; Higgins et al., 2018); Mg/Ca (Higgins and Schrag, 2006; Stewart et al., 2015); Sr/Ca (Stewart et al., 2015; Ahm et al., 2018; Higgins et al., 2018); $\delta^{238}U$ (Romaniello et al., 2013; Chen et al., 2018; Lau and Hardisty, 2022) $\delta^{34}S_{CAS}$ (Gill et al., 2008); I/Ca (Hardisty et al., 2014; Lau and Hardisty, 2022); Mn/Sr (Lohmann, 1988; Jacobsen and Kaufman, 1999; Ahm et al., 2018)

Process / Elemental Ratios		Major Element Isotope			Major Element		Trace Element Isotope		Trace element	
		Non-Redox Sensitive					Redox Sensitive			
Style	Environment	$\delta^{13}C$	$\delta^{18}O$	$\delta^{44}Ca$	Mg/Ca	Sr/Ca	$\delta^{238}U$	$\delta^{34}S_{CAS}$	I/Ca	Mn/Sr
Fluid buffered (open system)	Meteoric (oxygenated)	↓	↓↓	– or ↓	↓↓	↓	–	–	– or ↓	↑
	Seawater (oxygenated)	–	–	↑	–	↓	–	–	?	↑
	Reducing pore fluids	↓	–	–	–	–	↑↑	↑	↓	↑↑ ↑
	Dolomitization (evaporitic brine)	–	↑	↑↑↑	↑↑↑	↓↓	↓	–	–	↑
Sediment Buffered	Closed System	–	↓	–	–	↓	–	–	–	↑

345

346 The establishment of geochemical disequilibrium allowing for directional exchange
347 between the solid phase and sediment pore fluid can occur under either open or closed conditions
348 (Table 1). Open systems or fluid-buffered modes of diagenesis in which a high degree of exchange
349 occurs tend to be more chemically evolved than closed or sediment-buffered systems where pore
350 fluids are isolated (Higgins et al., 2018). Fluid-buffered diagenesis refers to the processes under
351 which high advective fluid flow through sediment pore space alters the precursor carbonate
352 compositions in the direction of the fluid composition (Higgins et al., 2018; Fantle et al. 2020).

353 Meteoric fluid-buffered diagenesis occurs when CO_2-rich freshwater derived from either
354 precipitation or runoff percolates through unsaturated pore space (Lohmann, 1988; Flugel, 2010).
355 Disequilibrium resulting from the mixing of different fluid compositions in the carbonate pore

space leads to dissolution and recrystallization of metastable polymorphs of calcite. Degassing of dissolved CO_2 results in the inorganic precipitation of carbonate, typically causing $\delta^{13}C$ of the bulk carbonate to decrease. Covariation between $\delta^{18}O$ and $\delta^{13}C$ is a conventional method of identifying early meteoric diagenesis, but it is not a definitive indicator in every setting (Swart and Oehlert, 2018, Fantle et al. 2020). Under meteoric fluid-buffered conditions secondary precipitates derive most of their calcium from the precursor material, so little calcium isotope fractionation occurs (Kimming and Holmden, 2017). Recrystallization with oxygenated fluids can also result in leaching of more soluble minor elements (e.g., Sr and Mg) (Stewart et al., 2015) while redox-sensitive trace-elements that are only soluble under reducing conditions may be retained (Lau and Hardisty, 2022). A reduction in I/Ca is predicted to occur under oxygenated fluid diagenesis only under very high fluid/rock ratios (Lau and Hardisty, 2022). Due to the low concentrations of U and SO_4^{2-} in fresh water, meteoric diagenesis is expected to lower carbonate-associated U and S concentrations but should not appreciably alter the $\delta^{34}S_{CAS}$ and $\delta^{238}U$ composition, as their dissolution does not impart fractionation (Gill et al., 2008; Zhang, et a 2020; Chen et al., 2021).

For both $\delta^{238}U$ and $\delta^{34}S_{CAS}$, the redox state of the pore water plays a more significant role in the degree of alteration. In downcore studies on the variation of $\delta^{238}U$ in modern carbonates undergoing active diagenesis, $\delta^{238}U$ values heavier than seawater have been attributed to the preferential incorporation of less soluble ^{238}U under sulfidic pore-water conditions (Romaniello et al., 2013; Chen et al., 2018). There are currently no post-depositional processes known to increase I/Ca values, but studies on recent and ancient carbonates report potential decreases under dolomitization (Hardisty et al., 2014; Hardisty et al., 2017; He et al., 2022b) and modeling demonstrates that I/Ca is highly sensitive to reducing fluids, more so than $\delta^{238}U$ and $\delta^{34}S_{CAS}$ (Lau and Hardisty, 2022). The Mn/Sr ratio can be used to qualitatively trace suboxic conditions due to

the differences in redox potential and solubility of Sr^{2+} and Mn^{2+} (Lohmann, 1988). An accepted threshold value that can indicate diagenetic alteration under some types of mildly reducing conditions is Mn/Sr greater than 0.2 mol/mol.

Dolomitization, where the fluid is a high-Mg brine, causes both Mg/Ca and $\delta^{44}Ca$ values to increase whereas Sr is lost due to exclusion from the dolomite lattice. Dolomitization may elevate Mn/Sr ratios via loss of Sr (Ahm et al., 2018) and decrease $\delta^{238}U$ due to leaching of ^{235}U (Romaniello et al., 2013). Brine composition is not expected to substantially alter $\delta^{34}S_{CAS}$, even if derived from sulfate evaporites, unless conditions are sulfidic (Shurr et al., 2021).

Under sediment-buffered conditions with little advective fluid flow, the dissolved Ca pool approaches the isotopic composition of the sediment (Fantle et al., 2010; Lau and Hardisty, 2022). Limited exchange between fluid and sediment undergoing dolomitization or aragonite-to-calcite neomorphism may alter the elemental composition, but the isotopic composition of the precursor is preserved due to the lack of any substantial material exchange (Ahm et al., 2018; Higgins et al., 2018). Sr concentrations may be lowered by sediment-buffered diagenesis if undergoing aragonite-to-calcite neomorphism (~1-4 mmol/mol) but not to the same extent as under fluid-buffered conditions (<1 mmol/mol) (Banner and Hanson, 1990; Ahm et al., 2018). An increase in Mn/Sr results from the loss of Sr. Increasing temperature with burial depth is largely responsible for decreasing $\delta^{18}O$ under sediment-buffered conditions (Murray and Swart, 2017).

4.2. Assessing possible diagenetic influence on redox proxies

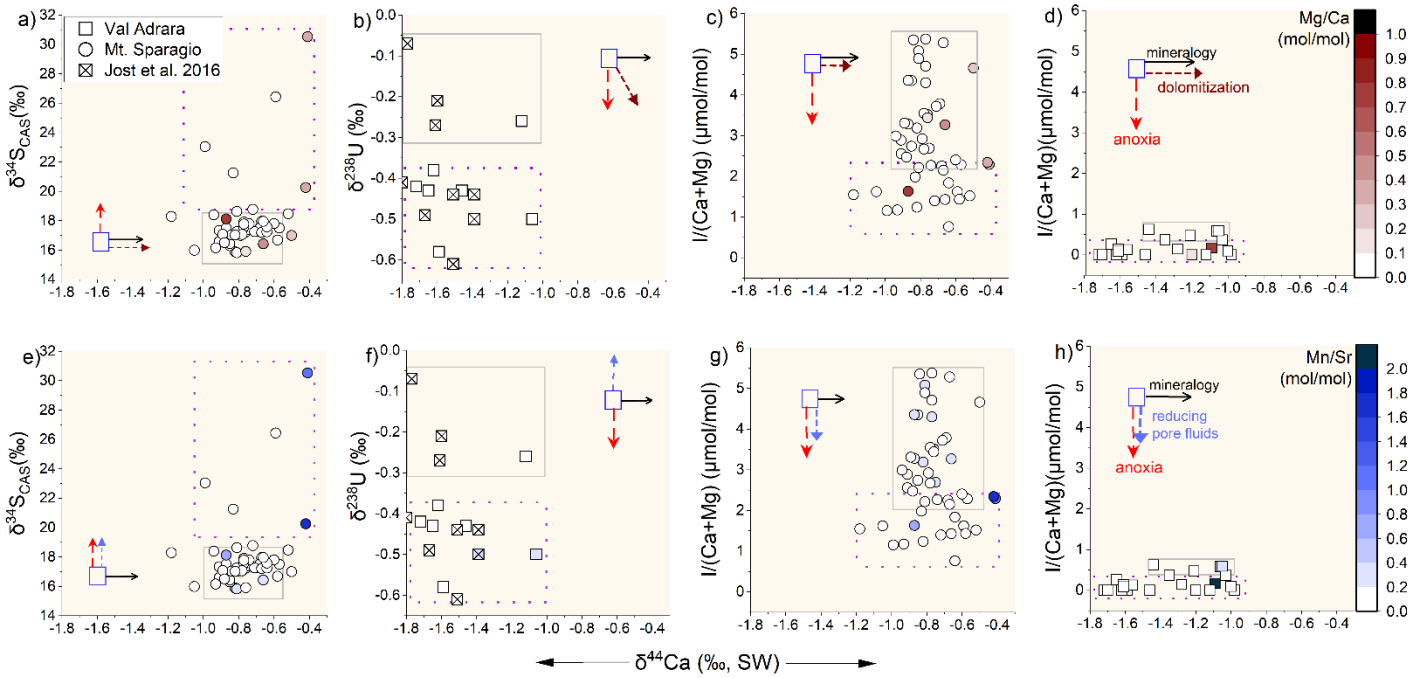

Figure 4: Cross plots of $\delta^{44}Ca$ against carbonate-based redox proxies. The top row (panels a-d) is color-coded by Mg/Ca ratio, indicative of dolomitization, where a value of 1.0 mol/mol is stoichiometric dolomite and the bottom row (panels e-h) is colored by Mn/Sr ratio, indicative of reducing pore fluids. The dotted boxes encompass the range of values during the positive carbon excursion. The solid grey boxes encompass most of the range of background (pre- and post-excursion) values. The small insert within each panel illustrates the expected trends of primary carbonate geochemical evolution due to dolomitization (brown dotted arrow), shifts in local or global anoxic conditions (red dotted line), reducing pore fluids (blue dotted arrow) and recrystallization from primary carbonate under fluid-buffered conditions (black solid arrow).

At Mount Sparagio, there is little covariation between $\delta^{44}Ca$ and $\delta^{34}S_{CAS}$ or I/Ca (Fig. 4a-c). The $\delta^{44}Ca$ values at Mount Sparagio are relatively high and a few points are elevated with respect to Mg/Ca (>0.5 mol/mol) or Mn/Sr (> 2.0 mol/mol), especially during the excursion, but there are no systematic correlations to indicate that dolomitization or reducing fluids significantly impacted the redox signals. Two out of five samples during the $\delta^{34}S_{CAS}$ excursion interval (Fig. 4e) show elevated Mn/Sr and Mg/Ca, and slightly higher $\delta^{44}Ca$. These two $\delta^{34}S_{CAS}$ values may have been post-depositionally elevated by reducing pore fluids, whereas other samples from the $\delta^{34}S_{CAS}$ excursion appear to be better preserved. At Val Adrara, the low $\delta^{238}U$ values during the

excursion, indicative of expanded global anoxia, have low Mg/Ca, Mn/Sr and $\delta^{44}Ca$ (Fig. 4b and 4f). Neither the new dataset nor that of Jost et al. (2016) reveals any covariation between $\delta^{238}U$ and $\delta^{44}Ca$, suggesting minimal diagenetic alteration of the $\delta^{238}U$ signal.

The decreases in I/Ca from background level into the excursion interval at both sites are not associated with any systematic increase in Mg/Ca, Mn/Sr, or $\delta^{44}Ca$ (Fig. 4c-d, g-h). Only one value at each site during the excursion interval is considerably elevated in either Mn/Sr or Mg/Ca to suggest potential alteration under reducing pore fluids. Therefore, the local deoxygenation trends recorded by I/Ca at both sites appears robust. At both sites, $\delta^{44}Ca$ becomes more variable during the excursion but does not trend more positive. Mount Sparagio shows higher Mn/Sr (up to 0.4 mol/mol) and $\delta^{44}Ca$ compared to Val Adrara, especially before the excursion interval, but there is no apparent trend. Because there is no process currently known to elevate I/Ca, these values at Mount Sparagio either reflect original redox conditions or possibly early oxygenated fluid-buffered diagenesis resulting in higher $\delta^{44}Ca$.

4.3. Carbonate Mineralogy

Table 2: Approximate end-member mineralogical element and isotopic compositions of carbonate precipitated from normal marine conditions. Sources: Sr/Ca and Mg/Ca (Morse and Mackenzie, 1990; Cicero and Lohmann 2001; Holcomb et al., 2009; Gussone et al., 2015), average $\delta^{44}Ca$ for modern carbonate platform aragonite sediment and high-Mg calcite from Higgins et al. (2018), low-Mg calcite from Marriott et al., (2004) and Blättler et al. (2012), calcite cement from Erhardt et al. (2020), and dolomite from Ahm et al. (2018).

	Aragonite	High-Mg Calcite	Low-Mg Calcite	Dolomite	Calcite Cement
Sr/Ca (mmol/mol)	7-10	1.5-4	1-1.5	<1.0	<1.0
Mg/Ca (mmol/mol)	2-6	6-50	2-4	100-1000	0.5-15
Modern $\delta^{44}Ca$ (SW, ‰)	-1.38	-1.13	-0.8	-0.68	-0.42

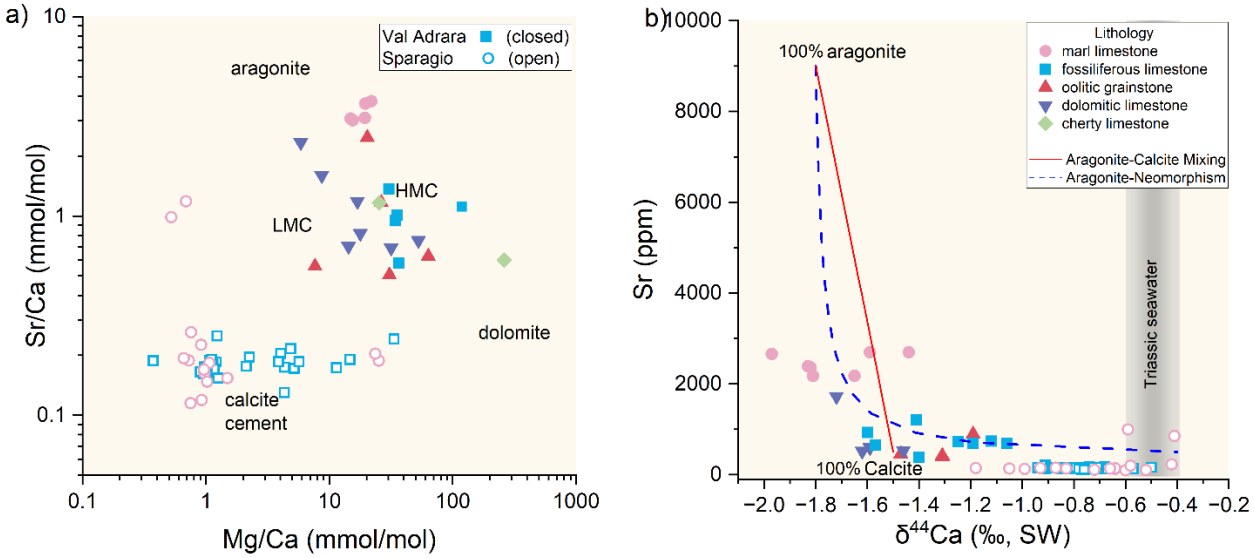

Figure 5: (a) Sr/Ca and Mg/Ca for Val Adrara (closed) and Mount Sparagio (open) colored by lithology. End-member carbonate mineralogy (e.g. dolomite, aragonite) labels placed in the approximate ranges of their compositions. LMC = low-magnesium calcite and HMC = high-magnesium calcite. (b) Cross plot of Sr content and $\delta^{44}Ca$ with a linear mixing model (red solid line) (Farkaš et al., 2017) between aragonite and calcite endmembers in Table 2 relative to Triassic seawater composition of -0.4 ‰ (Farkas et al. 2007;). In the model, aragonite has a Sr concentration of 8000 ppm and $\delta^{44}Ca$ of -1.8 ‰. Primary calcite has a Sr concentration of 500 ppm and $\delta^{44}Ca$ of -1.5 ‰. Dotted blue is line possible trajectory for fluid-buffered neomorphism of 100% aragonite with marine water of Triassic composition based a model by Lau et al. (2017).

We can further disentangle the diagenetic history and identify original carbonate source materials of these sites by plotting $\delta^{44}Ca$ against other isotopic and elemental ratios. Sr concentrations and Sr/Ca and Mg/Ca ratios together with $\delta^{44}Ca$ can be used to identify mineralogy and sources of carbonate (Fig. 5). Approximate end-member ratios for different carbonate mineralogies are given in Table 2. Samples from Val Adrara largely fall within the Sr/Ca vs Mg/Ca space for aragonite and high-magnesium calcite (HMC) (Fig. 5a) whereas samples from Mount Sparagio have very low Sr/Ca (<1mmol/mol) and high $\delta^{44}Ca$ throughout regardless of lithology (Gussone et al. 2020), indicative of recrystallization under fluid-buffered conditions. At Val Adrara, the marl limestone of the Malanotte Formation is elevated in Sr/Ca ratios relative to other

lithologies. The two samples with Sr/Ca greater than 1 mmol/mol at Mount Sparagio also belong to the marl layer within the TJ boundary interval (heights 203 and 209 m) (Fig. 2). Jost et al. (2016) recognized a large shift in Sr concentration within the Malanotte Formation, coincident with the negative excursion in $\delta^{44}Ca$ (Fig. 3). Increases in Sr/Ca ratios are observed at both sites in the new datasets (Fig. S1 and S2).

Here we evaluate the covariation in Sr content and $\delta^{44}Ca$ using a simple linear mixing model between aragonite and calcite endmembers, and plausible recrystallization pathways with different starting proportions of aragonite (Fig. 5b). Using a mass-balance approach, Jost et al. (2016) concluded that up to 80% in the negative $\delta^{44}Ca$ shift at Val Adrara in the Malanotte Formation could be attributed to an increase in aragonite in the original mineralogy. A greater contribution of aragonite to the original sediment could result from (1) migration of carbonate facies and mixing between deeper-water calcite and shallow-water aragonite sediments and/or (2) a shift in primary production favoring those that precipitate aragonitic skeletons (Farkas et al. 2016). At both Val Adrara and Mount Sparagio, the thin marl layer at the Triassic-Jurassic boundary interval occurs just before an inferred eustatic deepening indicated by a transition to carbonate mud-dominated lithology, therefore eustatic changes are unlikely to increase the proportion of aragonite. Pelagic calcifiers did not become abundant enough to be major sediment producers until the Middle Jurassic (Suzuki and Oba, 2015) and are therefore not a likely contributor to the change in aragonite observed Val Adrara. Benthic organisms with aragonite skeletons may be, on average, more susceptible to ocean acidification and rising carbonate compensation depth than their calcite-producing counterparts (Hautmann et al., 2008); however, only a modest relationship between skeletal mineralogy and extinction risk has been observed at the TJ boundary (Kiessling et al. 2007). Abundant megalodontid bivalves at Mount Sparagio (Todaro et al. 2018) could have

contributed to the slightly higher Sr/Ca values before their extinction (Fig. S1). Petrographic analysis on thin sections at Val Adrara revealed an increase in abundance of aragonitic calcareous algae within the Malanotte Formation (Singh et al., 2023). A shift in environmental conditions favoring growth of calcareous algae that disaggregated in fine-grained aragonitic needles could explain both the proportional increase in aragonite at Val Adrara and the texture of the sediment, but a closer inspection at Mount Sparagio would be needed to explain the regional extent of this marl layer.

The mixing of sediments from different carbonate sources (platform, pelagic, and meteoric cement) can be recognized by a linear covariation between $\delta^{13}C$ and $\delta^{44}Ca$ (Ahm et al., 2018; Higgins et al., 2018). At Val Adrara, there is a moderate covariation (Pearson's r = -0.70, p-value = 0.005) between $\delta^{13}C$ and $\delta^{44}Ca$ that suggests some mixing between sources, if not a reflection of open-system neomorphism, but the values stay in the region of marine deposition (Fig. 6). In contrast, there is no correlation in $\delta^{13}C$ and $\delta^{44}Ca$ values for samples from Mount Sparagio (Pearson's r = 0.08, p-value = 0.56) and most points fall near the zone of Triassic seawater value (Farkas et al., 2007). There is an apparent non-linear covariation of Sr and $\delta^{44}Ca$ at Val Adrara (Fig. 5b). Neomorphism of aragonite in fluid-buffered settings results in loss of Sr that is more rapid than diagenetic resetting of $\delta^{44}Ca$. None of the values at Val Adrara fall on the mixing curve but the marlstones with higher Sr content generally track the trajectory of recrystallization from an original sediment with high aragonite content. In contrast, the carbonates at Mount Sparagio are inferred to have been originally calcite, influenced by marine fluids. High $\delta^{44}Ca$ and low Sr content is also often found in marine cements (Cicero and Lohmann 2001; Gussone et al. 2020), and these cements may still capture primary seawater trace metal composition (Erhardt et al., 2020).

Carbonate mineralogy itself does not impart a considerable effect on incorporation of iodate into the carbonate (Feng and Redfern, 2018), but because iodine may be reduced but not completely excluded upon recrystallization (Hardisty et al. 2017), the overall I/Ca trends may reflect the conditions under which aragonite neomorphism occurred. It is impossible to separate fully the potential impacts of aragonite neomorphism at Val Adrara, fluid-buffered calcite diagenesis at Mount Sparagio, and primary redox variations, but we consider it likely that diagenetic effects did not completely eradicate the redox signals and there was a true difference in local conditions between the sections.

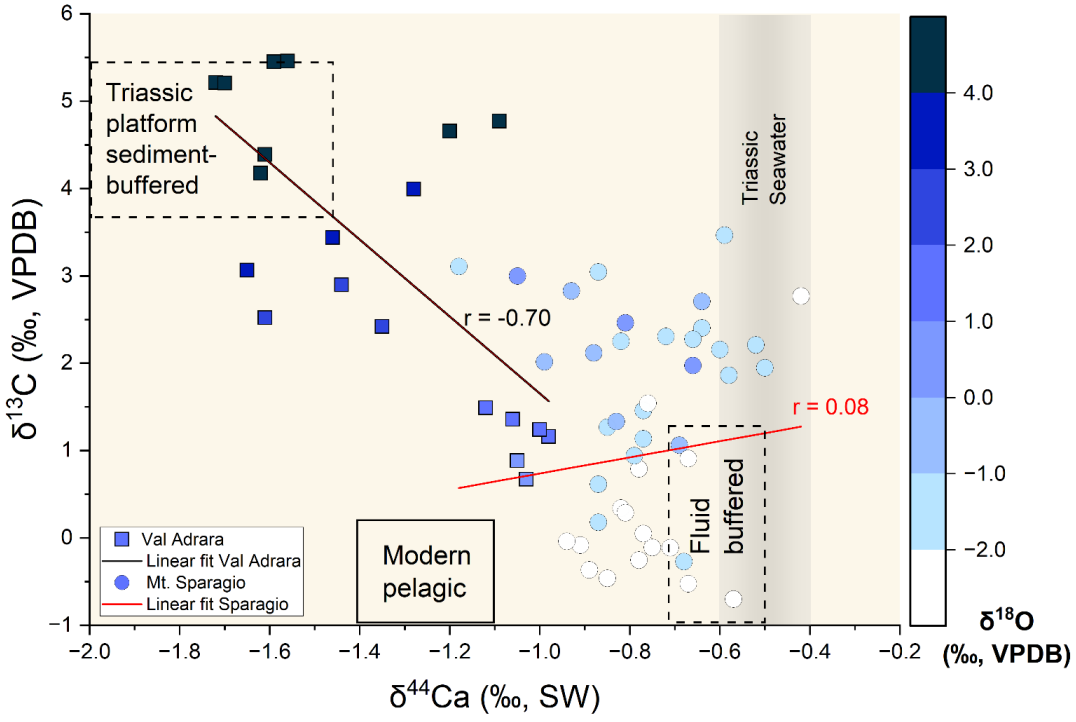

Figure 6: Covariation between bulk $\delta^{13}C_{carb}$ and $\delta^{44}Ca$ at Val Adrara (solid square) and Sparagio (open circles) colored by $\delta^{18}O$ value (Higgins et al., 2018). Dotted boxes are the approximate ranges isotopic composition of Triassic carbonate sources based on the estimated deviation from modern seawater value (grey bar) (Farkas et al. 2007). Regression lines (solid line) are given for data from Val Adrara (black) and Mt. Sparagio (red).

4.4 Potential Drivers of contrasting local redox conditions on the Tethys margin

I/Ca data for Val Adrara and Mount Sparagio suggest the existence of a redox gradient in the EES at the Triassic-Jurassic boundary, with dissolved oxygen decreasing northwards. A literature compilation for the redox conditions before and after extinction for several sites on the EES confirms that this gradient was of regional significance (Fig. 1c). To investigate the mechanisms leading to this N-S redox gradient in ocean anoxia and organic carbon burial, we analyzed the results of a 200 Ma simulation conducted with the Community Earth System Model (CESM) version 1.2.2 (Li et al., 2022a). While this simulation does not provide dissolved oxygen concentrations, the temperature, precipitation, and surface wind fields may shed light on regional atmospheric and oceanic circulations and thus help explain the contrasting paleoceanographic conditions in the northern vs southern EES.

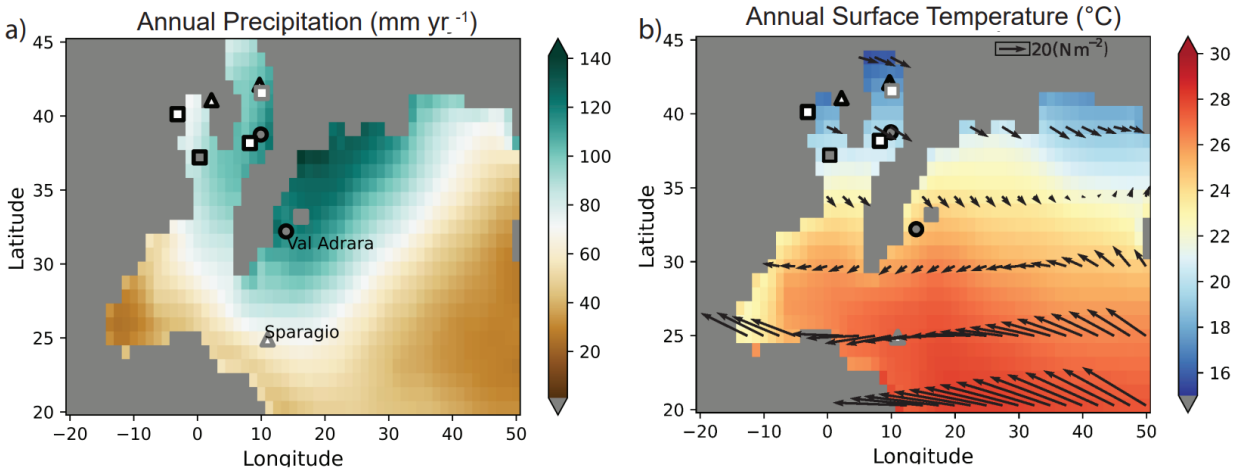

Figure 7: Climatic conditions on the EES. Annual precipitation (a), temperature and wind stress field (vectors) (b) simulations from CESM1.2.2 for the late Triassic (200 Ma; Li et al., 2022a). See Figure 1 for corresponding site descriptions and symbology.

There are notable differences in the hydroclimatic conditions between the two study sites on the EES (Fig. 7). Annual temperatures are slightly warmer at Mount Sparagio (~27°C) compared to Val Adrara (23-25°C), mainly resulting from differences in the paleolatitudes of the

two sections. This difference in ocean temperatures does not help explain the differences in ocean oxygenation. Because the solubility of oxygen in seawater decreases with increasing temperatures (Garcia and Gordon, 1992) the difference in sea-surface temperatures would, if anything, lead to a gradient opposite to what is observed, with higher dissolved oxygen concentrations in the (colder) northern part of the EES. This finding implies that other mechanisms must have been at play.

The explanation may be found in precipitation. The northern and southern regions of EES are simulated to have been in two different hydrological regimes, where Val Adrara was estimated to have received significantly more precipitation (up to 120 mm yr^{-1}) compared to Mount Sparagio (60-70 yr^{-1}) (Fig. 7a). This result is consistent with conceptual models for the regional circulation patterns throughout the Jurassic period which propose that increased atmospheric CO_2 enhanced the hydrologic cycle at northern latitudes, leading to more freshwater runoff from Laurasia into the restricted northern basins (van de Schootbrugge et al., 2020; Onoue et al., 2022). Density stratification due to an overlying low-salinity water mass may have established shallow subsurface dysoxia at Val Adrara. Val Adara is a shallow-water, high-energy location subject to frequent agitation producing the ooids and pelsparites that dominate the section. Deep-water anoxia spilling/upwelling into this shallow location may be an alternative scenario to be tested in future modeling study.

Regional ocean circulation may have reinforced the redox gradient on the EES. Ocean-atmosphere general circulation models simulating this Boreal-Tethys gradient during the Toarcian Ocean Anoxic Event (T-OAE, ~183 Ma) suggest that a limb from an equatorial gyre may have produced strong currents on the southern margin permitting vertical mixing (Ruvalcaba Baroni et al., 2018). These currents may have been weakened due to rough bathymetry and restriction within

the EES. Annual wind stress results from CESM for the Triassic-Jurassic boundary indicate that Mount Sparagio was in the path of high oncoming easterly wind bands (Fig. 7b), whereas Val Adrara was positioned in a zone of relatively low wind stress. Based on these patterns of wind stress, regional geography, and anoxic development within the EES water circulation pathways are proposed to explain the spatial pattern of oxygen depletion at the Triassic-Jurassic boundary (Fig. 1). Future work with a high-resolution, biogeochemistry-enabled model will be necessary to determine the precise mechanisms for this redox gradient, by quantifying the respective contributions of climate, ocean circulation, nutrient input to the ocean and possibly ocean gateways.

5. Conclusions

This study reports carbonate Ca isotope ratios from two Italian sequences, Mount Sparagio and Val Adrara, that record the end-Triassic mass extinction. Geochemical data are used to assess the role of diagenetic alteration and carbonate mineralogy on primary redox signals. The lack of covariation between diagenetic indicators (δ^{44}Ca, Mg/Ca, Mn/Sr) and redox proxies (I/Ca, $\delta^{34}S_{CAS}$ and δ^{238}U) suggests that some of the primary signal is likely preserved and the inferred differences in local redox between the two sites are legitimate, although diagenesis of inferred primary aragonite and calcite phases also contributes to geochemical variation. Earth system model reconstructions of the Triassic-Jurassic boundary suggest that the two sites were situated in different hydrological regimes and circulatory patterns could have primed the northern site, Val Adrara, for more reducing conditions. Looking forward, a coupled atmospheric-ocean model integrating biogeochemical tracers and bathymetry may offer a better appraisal of the potential drivers of the redox gradient. Paired with an assessment of pre- and post- extinction patterns at the

sites, we may gain an improved understanding of how physical environment interacted with marine life during the end-Triassic mass extinction.

Acknowledgments

This study was supported by NSF Frontier Research in Earth Sciences grant # 2121445 to Z.L., grant # 2121392 to J.L.P, and #2120406 to C.L.B. We thank A. Ridgwell and C. Ostrander for constructive feedback on the manuscript. Alex Dunhill, Simona Todaro and Pietro de Stefano are thanked for assistance with field sampling at the Monte Sparagio site. PCK was supported during this work by the TC Chamberlin Fellowship at the University of Chicago and by an NSF EAR postdoctoral fellowship (#2204376). AP acknowledges the support of the French *Agence Nationale de la Recherche* (ANR) under reference ANR-22-CE01-0003 (project ECO-BOOST) and of the programme TelluS of the *Institut National des Sciences de l'Univers*, CNRS (project ROSETTA). This is a contribution of UMR 6282 Biogéosciences Team 'SEDS'.

Open Research

Newly generated $\delta^{44}Ca$ and trace element data is available in the Supplementary material and upon request.

References

Ahm, A.S.C., Bjerrum, C.J., Blättler, C.L., Swart, P.K., and Higgins, J.A., 2018, Quantifying early marine diagenesis in shallow-water carbonate sediments: Geochimica et Cosmochimica Acta, v. 236, p. 140–159, doi:10.1016/j.gca.2018.02.042.

599 Algeo, T.J., and Li, C., 2020, Redox classification and calibration of redox thresholds in
600 sedimentary systems: Geochimica et Cosmochimica Acta, v. 287, p. 8–26,
601 doi:10.1016/j.gca.2020.01.055.

602 Atkinson, J.W., and Wignall, P.B. 2019. How quick was marine recovery after the end-
603 Triassic mass extinction and what role did anoxia play? Palaeogeography
604 Palaeoclimatology Palaeoecology 528, 99-119.

605 Bachan, A., Van De Schootbrugge, B., Fiebig, J., McRoberts, C.A., Ciarapica, G., and Payne,
606 J.L., 2012, Carbon cycle dynamics following the end-Triassic mass extinction:
607 constraints from paired δ13Ccarb and δ13Corg records: Geochemistry, Geophysics,
608 Geosystems, v. 13, p. 1–24, doi:10.1029/2012GC004150.

609 Bambach, R.K., 2006, Phanerozoic biodiversity mass extinctions: Annual Review of Earth
610 and Planetary Sciences, v. 34, p. 127–155,
611 doi:10.1146/annurev.earth.33.092203.122654.

612 Beith, S.J., Fox, C.P., Marshall, J.E.A., and Whiteside, J.H., 2021, Recurring photic zone
613 euxinia in the northwest Tethys impinged end-Triassic extinction recovery:
614 Palaeogeography, Palaeoclimatology, Palaeoecology, v. 584, p. 110680,
615 doi:10.1016/j.palaeo.2021.110680.

616 Bernardi, M., Gianolla, P., Petti, F.M., Mietto, P., and Benton, M.J., 2018, Dinosaur
617 diversification linked with the Carnian Pluvial Episode: Nature Communications, v. 9,
618 doi:10.1038/s41467-018-03996-1.

Blackburn, T.J., Olsen, P.E., Bowring, S.A., McLean, N.M., Kent, D. V., Puffer, J., McHone, G., Rasbury, E.T., and Et-Touhami, M., 2013, Zircon U-Pb geochronology links the end-Triassic extinction with the central Atlantic magmatic province: Science, v. 340, p. 941–945, doi:10.1126/science.1234204.

Blättler, C.L., Henderson, G.M., and Jenkyns, H.C., 2012, Explaining the Phanerozoic Ca isotope history of seawater: Geology, v. 40, p. 843–846, doi:10.1130/G33191.1.

Bowman, C.N., Young, S.A., Kaljo, D., Eriksson, M.E., Them, T.R., Hints, O., Martma, T., and Owens, J.D., 2019, Linking the progressive expansion of reducing conditions to a stepwise mass extinction event in the late Silurian oceans: Geology, v. 47, p. 968–972, doi:10.1130/G46571.1.

Chandler, M.A., Rind, D., and Ruedy, R., 1992, Pangaean climate during the early Jurassic: GCM simulations and the sedimentary record of paleoclimate: Geological Society of America Bulletin, v. 104, p. 543–559.

Chen, X., Romaniello, S.J., Herrmann, A.D., Hardisty, D., Gill, B.C., and Anbar, A.D., 2018, Diagenetic effects on uranium isotope fractionation in carbonate sediments from the Bahamas: Geochimica et Cosmochimica Acta, v. 237, p. 294–311, doi:10.1016/j.gca.2018.06.026.

Dal Corso, J., Mills, B.J.W., Chu, D., Newton, R.J., and Song, H., 2022, Background Earth system state amplified Carnian (Late Triassic) environmental changes: Earth and Planetary Science Letters, v. 578, p. 117321, doi:10.1016/j.epsl.2021.117321.

639 Dera, G., Neige, P., Dommergues, J.-L., & Brayard, A., 2011, Ammonite paleobiogeography
640 during the Pliensbachian–Toarcian crisis (Early Jurassic) reflecting paleoclimate,
641 eustasy, and extinctions. Global and Planetary Change, 78(3), 92–105.

642 Dera, G., and Donnadieu, Y., 2012, Modeling evidences for global warming, Arctic seawater
643 freshening, and sluggish oceanic circulation during the Early Toarcian anoxic event:
644 Paleoceanography, v. 27, p. 1–15, doi:10.1029/2012PA002283.

645 Dickson, A.J., Cohen, A.S., and Coe, A.L., 2012, Seawater oxygenation during the
646 Paleocene-Eocene Thermal Maximum: Geology, v. 40, p. 639–642,
647 doi:10.1130/G32977.1.

648 Dore, A., 1991, The structural foundation and evolution of Mesozoic seaways between
649 Europe and the Arctic: Palaeogeography, Palaeoclimatology, Palaeoecology, v. 87, p.
650 441–492.

651 Elderfield, H., and Truesdale, V.W., 1980, On the biophilic nature of iodine in seawater: Earth
652 and Planetary Science Letters, v. 50, p. 105–114, doi:10.1016/0012-821X(80)90122-3.

653 Fantle, M.S., Barnes, B.D., and Lau, K. V., 2020, The Role of Diagenesis in Shaping the
654 Geochemistry of the Marine Carbonate Record: Annual Review of Earth and Planetary
655 Sciences, v. 48, p. 549–583, doi:10.1146/annurev-earth-073019-060021.

656 Fantle, M.S., and DePaolo, D.J., 2007, Ca isotopes in carbonate sediment and pore fluid
657 from ODP Site 807A: The Ca2+(aq)-calcite equilibrium fractionation factor and
658 calcite recrystallization rates in Pleistocene sediments: Geochimica et
659 Cosmochimica Acta, v. 71, p. 2524–2546, doi:10.1016/j.gca.2007.03.006.

Fantle, M.S., and Higgins, J., 2014, The effects of diagenesis and dolomitization on Ca and Mg isotopes in marine platform carbonates: Implications for the geochemical cycles of Ca and Mg: Geochimica et Cosmochimica Acta, v. 142, p. 458–481, doi:10.1016/j.gca.2014.07.025.

Farkaš, J., Frýda, J., and Holmden, C., 2017, Corrigendum to "Calcium isotope constraints on the marine carbon cycle and CaCO3 deposition during the late Silurian (Ludfordian) positive δ13C excursion" [Earth Planet. Sci. Lett. 451 (2016) 31–40]: Earth and Planetary Science Letters, v. 469, p. 170–171, doi:10.1016/j.epsl.2017.04.013.

Feng, X., and Redfern, S.A.T., 2018, Iodate in calcite, aragonite and vaterite CaCO3: Insights from first-principles calculations and implications for the I/Ca geochemical proxy: Geochimica et Cosmochimica Acta, v. 236, p. 351–360, doi:10.1016/j.gca.2018.02.017.

Fike, D.A., Bradley, A.S., and Rose, C. V., 2015, Rethinking the ancient sulfur cycle: Annual Review of Earth and Planetary Sciences, v. 43, p. 593–622, doi:10.1146/annurev-earth-060313-054802.

Gill, B.C., Lyons, T.W., and Frank, T.D., 2008, Behavior of carbonate-associated sulfate during meteoric diagenesis and implications for the sulfur isotope paleoproxy: Geochimica et Cosmochimica Acta, v. 72, p. 4699–4711, doi:10.1016/j.gca.2008.07.001.

679 Gill, B.C., Lyons, T.W., and Jenkyns, H.C., 2011, A global perturbation to the sulfur cycle
680 during the Toarcian Oceanic Anoxic Event: Earth and Planetary Science Letters, v. 312,
681 p. 484–496, doi:10.1016/j.epsl.2011.10.030.

682 Griffith, E.M., Fantle, M.S., Eisenhauer, A., Paytan, A., and Bullen, T.D., 2015, Effects of
683 ocean acidification on the marine calcium isotope record at the Paleocene-Eocene
684 Thermal Maximum: Earth and Planetary Science Letters, v. 419, p. 81–92,
685 doi:10.1016/j.epsl.2015.03.010.

686 Gussone, N., Ahm, A.S.C., Lau, K. V., and Bradbury, H.J., 2020, Calcium isotopes in deep
687 time: Potential and limitations: Chemical Geology, v. 544, p. 119601,
688 doi:10.1016/j.chemgeo.2020.119601.

689 Hardisty, D.S., Lu, Z., Planavsky, N.J., Bekker, A., Philippot, P., Zhou, X., and Lyons, T.W.,
690 2014, An iodine record of Paleoproterozoic surface ocean oxygenation: p. 619–622,
691 doi:10.1130/G35439.1.

692 Hautmann, M. 2006, Shell mineralogical trends in epifaunal Mesozoic bivalves and their
693 relationship to seawater chemistry and atmospheric carbon dioxide concentration,
694 Facies, 52(3), 417–433, doi:10.1007/s10347-005-0029-x.

695 He, T., Dal Corso, J., Newton, R.J., Wignall, P.N., Mills, B.J.W., Todaro, S., Di Stefano, P.,
696 Turner, E.C., Jamieson, R.A., Randazzo, V., Rigo, M., Jones, R.E., Dunhill, A. M., 2020,
697 An enormous sulfur isotope excursion indicates marine anoxia during the end-Triassic
698 mass extinction: Science Advances, v. 6, p. 2–10, doi:10.1126/sciadv.abb6704.

He, T., Newton, R.J., Wignall, P.B., Reid, S., Dal Corso, J., Takahashi, S., Wu, H., Todaro, S., Di Stefano, P., Randazzo, V., Rigo, M., Dunhill, A. M., 2022, Shallow ocean oxygen decline during the end-Triassic mass extinction: Global and Planetary Change, v. 210, p. 103770, doi:10.1016/j.gloplacha.2022.103770.

He, R., Elrick, M., Day, J., Lu, W., and Lu, Z., 2022, Devonian upper ocean redox trends across Laurussia: Testing potential influences of marine carbonate lithology on bulk rock I / Ca signals: , p. 1–12, doi:10.3389/fmars.2022.874759.

He, R., Lu, W., Junium, C.K., Ver Straeten, C.A., and Lu, Z., 2020, Paleo-redox context of the Mid-Devonian Appalachian Basin and its relevance to biocrises: Geochimica et Cosmochimica Acta, v. 287, p. 328–340, doi:10.1016/j.gca.2019.12.019.

Hesselbo, S.P., Robinson, S.A., Surlyk, F., and Piasecki, S., 2002, Terrestrial and marine extinction at the Triassic-Jurassic boundary synchronized with major carbon-cycle perturbation: A link to initiation of massive volcanism? Geology, v. 30, p. 251–254, doi:10.1130/0091-7613(2002)030.

Higgins, J.A., Blättler, C.L., Lundstrom, E.A., Santiago-Ramos, D.P., Akhtar, A.A., Crüger Ahm, A-S., Bialik, O., Holmden, C., Bradbury, H., Murray, S.T., Swart, P.K., 2018, Mineralogy, early marine diagenesis, and the chemistry of shallow-water carbonate sediments: Geochimica et Cosmochimica Acta, v. 220, p. 512–534, doi:10.1016/j.gca.2017.09.046.

718 Higgins, J.A., and Schrag, D.P., 2006, Beyond methane: Towards a theory for the Paleocene-
719 Eocene Thermal Maximum: Earth and Planetary Science Letters, v. 245, p. 523–537,
720 doi:10.1016/j.epsl.2006.03.009.

721 Hodges, M.S., and Stanley, G.D., 2015. North American coral recovery after the end-Triassic
722 mass extinction, New York Canyon, Nevada, USA. GSA Today 25 (10), 4–9.

723 Iannace, A., and Frisia, S., 1994, Changing dolomitization styles from Norian to Rhaetian in
724 the southern Tethys realm: Spec. Pbuis Int. Ass. Sediment, v. 21, p. 75–89.
725 10.1002/9781444304077.ch6.

726 Jacobsen, S.B., and Kaufman, A.J., 1999, The Sr, C and O isotopic evolution of
727 Neoproterozoic seawater: Chemical Geology, v. 161, p. 37–57, doi:10.1016/S0009-
728 2541(99)00080-7.

729 Jacobson, A.D., and Holmden, C., 2008, δ44Ca evolution in a carbonate aquifer and its
730 bearing on the equilibrium isotope fractionation factor for calcite: Earth and
731 Planetary Science Letters, v. 270, p. 349–353, doi:10.1016/j.epsl.2008.03.039.

732 Jadoul, F., and Galli, M.T., 2008, The Hettangian shallow water carbonates after the
733 Triassic/Jurassic biocalcification crisis: The Albenza Formation in the western southern
734 Alps: Rivista Italiana di Paleontologia e Stratigrafia, v. 114, p. 453–470,
735 doi:10.13130/2039-4942/5911.

736 Jin, X., Gianolla, P., Shi, Z., Franceschi, M., Caggiati, M., Du, Y., and Preto, N., 2020,
737 Synchronized changes in shallow water carbonate production during the Carnian Pluvial

738 Episode (Late Triassic) throughout Tethys: Global and Planetary Change, v. 184, p.
739 103035, doi:10.1016/j.gloplacha.2019.103035.

740 Jost, 2016, Additive effects of acidification and mineralogy on calcium isotopes in
741 Triassic/Jurassic boundary limestones: Geochemistry Geophysics Geosystems, v. 17, p.
742 1312–1338, doi:10.1002/2015GC006205.

743 Jost, A.B., Bachan, A., van de Schootbrugge, B., Lau, K. V., Weaver, K.L., Maher, K., and
744 Payne, J.L., 2017, Uranium isotope evidence for an expansion of marine anoxia during
745 the end-Triassic extinction: Geochemistry, Geophysics, Geosystems, v. 18, p. 3093–
746 3108, doi:10.1002/2017GC006941.

747 Judd, E.J., Ghattacharya, T., and Ivany, L.C., 2020, A Dynamical Framework for Interpreting
748 Ancient Sea Surface Temperatures Geophysical Research Letters:,
749 doi:10.1029/2020GL089044.

750 Kampschulte, A., and Strauss, H., 2004, The sulfur isotopic evolution of Phanerozoic
751 seawater based on the analysis of structurally substituted sulfate in carbonates: v. 204,
752 p. 255–286, doi:10.1016/j.chemgeo.2003.11.013.

753 Kiessling, W., Aberhan, M., Brenneis, B., and Wagner, P.J., 2007, Extinction trajectories of
754 benthic organisms across the Triassic-Jurassic boundary: Palaeogeography,
755 Palaeoclimatology, Palaeoecology,v.244, p. 201–222, doi:10.1016/j.palaeo.2006.06.029

756 Kimmig, S.R., and Holmden, C., 2017, Multi-proxy geochemical evidence for primary
757 aragonite precipitation in a tropical-shelf ‘calcite sea ’ during the Hirnantian glaciation

ScienceDirect Multi-proxy geochemical evidence for primary aragonite precipitation in a tropical-shelf ‘ calcite sea:, doi:10.1016/j.gca.2017.03.010.

Lau, K. V. et al., 2017, The influence of seawater carbonate chemistry, mineralogy, and diagenesis on calcium isotope variations in Lower-Middle Triassic carbonate rocks: Chemical Geology, v. 471, p. 13–37, doi:10.1016/j.chemgeo.2017.09.006.

Lau, K. V., and Hardisty, D.S., 2022, Modeling the impacts of diagenesis on carbonate paleoredox proxies: Geochimica et Cosmochimica Acta, v. 337, p. 123–139, doi:10.1016/j.gca.2022.09.021.

Li, J., Song, H., Tian, L., Bond, D. P. G., Song, H., Du, Y., et al. (2022). Dynamic ocean redox conditions during the end-Triassic mass extinction: Evidence from pyrite framboids. *Global and Planetary Change*, *218*(May), 103981. https://doi.org/10.1016/j.gloplacha.2022.103981

Li, X. et al., 2022, A high-resolution climate simulation dataset for the past 540 million years: Scientific Data, v. 9, p. 1–10, doi:10.1038/s41597-022-01490-4.

Lohmann, C.K., 1988, Geochemical Patterns of Meteoric Diagenetic Systems and their Application to Studies of Paleokarst, *in* Choquestte, P.W. and James, N.. eds., Paleokarst, Springer-Verlag, p. 58–80.

Lu, Z., B.A.A., H., Hillenbrand, C., Zhou, X., Thomas, E., Gutchess, K.M., Lu, W., Jones, L., and Rickaby, R.E.M., 2016, Oxygen depletion recorded in upper waters of the glacial Southern Ocean: Nature Communications, v. 48, p. 829–834, doi:10.1038/pj.2016.37.

778 Lu, Z., Jenkyns, H.C., and Rickaby, R.E.M., 2010, Iodine to calcium ratios in marine
779 carbonate as a paleo-redox proxy during oceanic anoxic events: Geology, v. 38, p. 1107–
780 1110, doi:10.1130/G31145.1.

781 Lu, Z., Lu, W., Rickaby, R.E.M., and Thomas, E., 2020, Earth History of Oxygen and the
782 iprOxy: Cambridge, Cambridge University Press, doi:10.1017/9781108688604.

783 Luo, G., Richoz, S., van de Schootbrugge, B., Algeo, T.J., Xie, S., Ono, S., and Summons,
784 R.E., 2018, Multiple sulfur-isotopic evidence for a shallowly stratified ocean following
785 the Triassic-Jurassic boundary mass extinction: Geochimica et Cosmochimica Acta, v.
786 231, p. 73–87, doi:10.1016/j.gca.2018.04.015.

787 Marriott, C.S., Henderson, G.M., Belshaw, N.S., and Tudhope, A.W., 2004, Temperature
788 dependence of δ7Li, δ44Ca and Li/Ca during growth of calcium carbonate: Earth
789 and Planetary Science Letters, v. 222, p. 615–624, doi:10.1016/j.epsl.2004.02.031.

790 McArthur, J.M., 2019, Early Toarcian black shales: A response to an oceanic anoxic event or
791 anoxia in marginal basins? Chemical Geology, v. 522, p. 71–83,
792 doi:10.1016/j.chemgeo.2019.05.028.

793 Oehlert, A.M., and Swart, P.K., 2014, Interpreting carbonate and organic carbon isotope
794 covariance in the sedimentary record: Nature Communications, v. 5, p. 1–7,
795 doi:10.1038/ncomms5672.

796 Onoue, T., Michalík, J., Shirozu, H., Yamashita, M., Yamashita, K., Kusaka, S., and Soda,
797 K., 2022, Extreme continental weathering in the northwestern Tethys during the end-

Triassic mass extinction: Palaeogeography, Palaeoclimatology, Palaeoecology, v. 594, p. 110934, doi:10.1016/j.palaeo.2022.110934.

Owens, J.D., Gill, B.C., Jenkyns, H.C., Bates, S.M., Severmann, S., Kuypers, M.M.M., Woodfine, R.G., and Lyons, T.W., 2013, Sulfur isotopes track the global extent and dynamics of euxinia during Cretaceous oceanic anoxic event 2: Proceedings of the National Academy of Sciences of the United States of America, v. 110, p. 18407–18412, doi:10.1073/pnas.1305304110.

Paris, G., Beaumont, V., Bartolini, A., Clémence, M. E., Gardin, S., & Page, K. (2010). Nitrogen isotope record of a perturbed paleoecosystem in the aftermath of the end-Triassic crisis, Doniford section, SW England. *Geochemistry, Geophysics, Geosystems*, *11*(8), 1–15. https://doi.org/10.1029/2010GC003161

Razionale, D., Bryant, R.N., and Blättler, C.L., 2022, Adapting automated instrumentation for high-throughput calcium isotope measurements by multi-collector inductively coupled plasma mass spectrometry: Rapid Communications in Mass Spectrometry, v. 36, p. 1–13, doi:10.1002/rcm.9249.

Richoz, S. et al., 2012, Hydrogen sulphide poisoning of shallow seas following the end-Triassic extinction: Nature Geoscience, v. 5, p. 662–667, doi:10.1038/ngeo1539.

Rigo, M., Trotter, J.A., Preto, N., and Williams, I.S., 2012, Oxygen isotopic evidence for late Triassic monsoonal upwelling in the northwestern Tethys: Geology, v. 40, p. 515–518, doi:10.1130/G32792.1.

Rohl, and Schmid-Rohl, 2011, Lower Toarcian (Upper Liassic) Black Shales of the Central European Epicontinental Basin: A Sequence Stratigraphic Case Study from the Sw German Posidonia Shale: Deposition of Organic-Carbon-Rich Sediments: Models, p. 165–189, doi:10.2110/pec.05.82.0165.

Romaniello, S.J., Herrmann, A.D., and Anbar, A.D., 2013, Uranium concentrations and 238U/235U isotope ratios in modern carbonates from the Bahamas: Assessing a novel paleoredox proxy: Chemical Geology, v. 362, p. 305–316, doi:10.1016/j.chemgeo.2013.10.002.

Ruvalcaba Baroni, I., Pohl, A., van Helmond, N.A.G.M., Papadomanolaki, N.M., Coe, A.L., Cohen, A.S., van de Schootbrugge, B., Donnadieu, Y., and Slomp, C.P., 2018, Ocean Circulation in the Toarcian (Early Jurassic): A Key Control on Deoxygenation and Carbon Burial on the European Shelf: Paleoceanography and Paleoclimatology, v. 33, p. 994–1012, doi:10.1029/2018PA003394.

Santantonio, M., and Carminati, E., 2011, Jurassic rifting evolution of the Apennines and Southern Alps (Italy): Parallels and differences: Bulletin of the Geological Society of America, v. 123, p. 468–484, doi:10.1130/B30104.1.

Schoene, B., Guex, J., Bartolini, A., Schaltegger, U., and Blackburn, T.J., 2010, Correlating the end-Triassic mass extinction and flood basalt volcanism at the 100 ka level: Geology, v. 38, p. 387–390, doi:10.1130/G30683.1.

Sellwood, B.W., and Valdes, P.J., 2006, Mesozoic climates: General circulation models and the rock record: v. 190, p. 269–287, doi:10.1016/j.sedgeo.2006.05.013.

839 Sha, J. 2002, Hispanic Corridor formed as early as Hettangian: On the basis of bivalve fossils:
840 Chinese Scientific Bulletin, v. 47, p. 1–4.

841 Singh, P., Lu, W., Lu, Z., Jost, A.B., Lau, K., Bachan, A., Schootbrugge, B. Van De, and
842 Payne, J.L., 2023, Reduction in animal abundance and oxygen availability during and
843 after the end-Triassic mass extinction: , p. 175–192, doi:10.1111/gbi.12533.

844 Song, H. et al., 2021, Conodont calcium isotopic evidence for multiple shelf acidification
845 events during the Early Triassic: Chemical Geology, v. 562, p. 120038,
846 doi:10.1016/j.chemgeo.2020.120038.

847 Stewart, J.A., Gutjahr, M., Pearce, F., Swart, P.K., and Foster, G.L., 2015, Boron during
848 meteoric diagenesis and its potential implications for Marinoan snowball Earth δ11B-
849 pH excursions: Geology, v. 43, p. 627–630, doi:10.1130/G36652.1.

850 Suzuki N, Oba M (2015) Oldest fossil records of marine protists and the geologic history
851 toward the establishment of the modern-type marine protist world. In: Ohtsuka S et al.
852 (eds) Marine protists: diversity and dynamics. Springer, Tokyo, pp 359–394

853 Swart, P.K., and Oehlert, A.M., 2018, Revised interpretations of stable C and O patterns in
854 carbonate rocks resulting from meteoric diagenesis: Sedimentary Geology, v. 364, p.
855 14–23, doi:10.1016/j.sedgeo.2017.12.005.

856 Tang, J., Dietzel, M., Böhm, F., Köhler, S.J., and Eisenhauer, A., 2008, Sr2+/Ca2+ and
857 44Ca/40Ca fractionation during inorganic calcite formation: II. Ca isotopes: Geochimica
858 et Cosmochimica Acta, v. 72, p. 3733–3745, doi:10.1016/j.gca.2008.05.033.

Todaro, S., Rigo, M., Randazzo, V., and Di Stefano, P., 2018, The end-Triassic mass extinction: A new correlation between extinction events and $\delta^{13}C$ fluctuations from a Triassic-Jurassic peritidal succession in western Sicily: Sedimentary Geology, v. 368, p. 105–113, doi:10.1016/j.sedgeo.2018.03.008.

van de Schootbrugge, B., Payne, J.L., Tomasovych, A., Pross, J., Fiebig, J., Benbrahim, M., Föllmi, K.B., and Quan, T.M., 2008, Carbon cycle perturbation and stabilization in the wake of the Triassic-Jurassic boundary mass-extinction event: Geochemistry, Geophysics, Geosystems, v. 9, doi:10.1029/2007GC001914.

van de Schootbrugge, B., Bachan, A., Suan, G., Richoz, S., and Payne, J.L., 2013, Microbes, mud and methane: Cause and consequence of recurrent early Jurassic anoxia following the end-Triassic mass extinction: Palaeontology, v. 56, p. 685–709, doi:10.1111/pala.12034.

van de Schootbrugge, B., Houben, A.J.P., Ercan, F.E.Z., Verreussel, R., Kerstholt, S., Janssen, N.M.M., Nikitenko, B., and Suan, G., 2020, Enhanced Arctic-Tethys connectivity ended the Toarcian Oceanic Anoxic Event in NW Europe: Geological Magazine, v. 157, p. 1593–1611, doi:10.1017/S0016756819001262.

White, D.A., Elrick, M., Romaniello, S., and Zhang, F., 2018, Global seawater redox trends during the Late Devonian mass extinction detected using U isotopes of marine limestones: Earth and Planetary Science Letters, v. 503, p. 68–77, doi:10.1016/j.epsl.2018.09.020.

879 Wignall, P.B., and Atkinson, J. 2020. A two-phase end-Triassic mass extinction. Earth-
880 Science Reviews 208, 103282.

881 Young, E.D., Galy, A., and Nagahara, H., 2002, Kinetic and equilibrium mass-dependent
882 isotope fractionation laws in nature and their geochemical and cosmochemical
883 significance: Geochimica et Cosmochimica Acta, v. 66, p. 1095–1104,
884 doi:10.1016/S0016-7037(01)00832-8.

885 Zacaï, A., Brayard, A., Dommergues, J.-L., Meister, C., Escarguel, G., Laffont, R., et al.
886 (2016). Gauging scale effects and biogeographical signals in similarity distance decay
887 analyses: An Early Jurassic ammonite case study. Palaeontology, 59(5), 671–687.

888 Zhang, F. et al., 2020, Uranium isotopes in marine carbonates as a global ocean paleoredox
889 proxy: A critical review: Geochimica et Cosmochimica Acta, v. 287, p. 27–49,
890 doi:10.1016/j.gca.2020.05.011.

891